New host for carbon in the deep Earth

Eglantine Boulard[a,1], Alexandre Gloter[b], Alexandre Corgne[a,c], Daniele Antonangeli[a], Anne-Line Auzende[a], Jean-Philippe Perrillat[d,e], François Guyot[a], and Guillaume Fiquet[a]

[a]Institut de Minéralogie et de Physique des Milieux Condensés, Institut de Physique du Globe de Paris, Université Pierre et Marie Curie, Unité Mixte de Recherche (UMR) Centre National de la Recherche Scientifique (CNRS) 7590, Université Paris Diderot, 4 place Jussieu, 75005 Paris, France; [b]Laboratoire de Physique des Solides, Université Paris Sud 11, CNRS UMR 8502, F-91405 Orsay, France; [c]Institut de Recherche en Astrophysique et Planétologie, UMR 5277 Université de Toulouse—CNRS, 14 avenue Edouard Belin, 31400 Toulouse, France; [d]European Synchrotron Radiation Facility, B.P. 220, 38043 Grenoble cedex, France; and [e]Université Claude Bernard Lyon 1, Laboratoire de Sciences de la Terre, UMR 5570 CNRS, 2 rue Raphaël Dubois, 69622 Villeurbanne, France

Edited by David Walker, Columbia University, Palisades, NY, and approved February 4, 2011 (received for review November 10, 2010)

The global geochemical carbon cycle involves exchanges between the Earth's interior and the surface. Carbon is recycled into the mantle via subduction mainly as carbonates and is released to the atmosphere via volcanism mostly as CO_2. The stability of carbonates versus decarbonation and melting is therefore of great interest for understanding the global carbon cycle. For all these reasons, the thermodynamic properties and phase diagrams of these minerals are needed up to core mantle boundary conditions. However, the nature of C-bearing minerals at these conditions remains unclear. Here we show the existence of a new Mg-Fe carbon-bearing compound at depths greater than 1,800 km. Its structure, based on three-membered rings of corner-sharing $(CO_4)^{4-}$ tetrahedra, is in close agreement with predictions by first principles quantum calculations [Oganov AR, et al. (2008) Novel high-pressure structures of $MgCO_3$, $CaCO_3$ and CO_2 and their role in Earth's lower mantle. *Earth Planet Sci Lett* 273:38–47]. This high-pressure polymorph of carbonates concentrates a large amount of $Fe^{(III)}$ as a result of intracrystalline reaction between $Fe^{(II)}$ and $(CO_3)^{2-}$ groups schematically written as $4FeO + CO_2 \rightarrow 2Fe_2O_3 + C$. This results in an assemblage of the new high-pressure phase, magnetite and nanodiamonds.

diamond | Earth mantle | phase transition | experimental petrology | redox interaction

Carbonates are the main form of carbon-bearing minerals that can be transported deep in the Earth's mantle via subduction of the oceanic lithosphere (1). This subducted component is considered to contribute significantly to the lower mantle carbon (C) reservoir along with primordial C (2, 3). Because of its very low solubility in deep Earth's minerals (4, 5), C is likely to be present as a separate phase, either as carbonates or as diamonds. Several studies have suggested that magnesium carbonate (magnesite) could become the main host for C at depth at the expense of calcite and dolomite (6–8). Other models proposed that carbonates in equilibrium with peridotite would become reduced into diamonds at lower mantle conditions (9). However, as observed in the upper mantle, heterogeneities of the lower mantle redox state probably exist: For instance, subduction zones are made of more oxidized materials (10) that could survive on long time scales. Coexistence of both reduced and oxidized species in the deep Earth is also suggested by examples such as CO_2-rich kimberlitic magmas that have transported diamonds to the surface (11, 12), and some carbonate inclusions that were found in diamonds from the lower mantle (13, 14). Results of high-pressure experiments on carbonate stability suggest that the rhombohedral structure of $MgCO_3$ magnesite is stable up to 115 GPa at 2,000–3,000 K, but that it adopts a new structure at higher pressures (8). However, first-principle calculations predicted magnesite transformations into phases built with $(CO_4)^{4-}$ tetrahedral groups at 82 GPa, and a transformation into pyroxene-like structures is expected at 160 GPa (15–17). Considering the average Fe/Mg molar ratio of 0.12 in the Earth's mantle, the composition of carbonates is likely to lie between those of magnesite and the iron end member $FeCO_3$ siderite, the two phases being known to form a continuous solid solution. So far, transformations of iron-bearing carbonates have rarely been examined. Siderite is known to be stable up to at least 47 GPa and 2,000 K (18), and up to 90 GPa at ambient temperature (19). Overall, the structural behavior of siderite and magnesite end members is thought to be similar because the effect of size mismatch between $Fe^{(II)}$ and Mg atoms is compensated by a spin transition in $Fe^{(II)}$ (19, 20).

Results

Consistent conclusions about the stability of a high-pressure carbon-bearing compound can be drawn for both $MgCO_3$ and the assemblage $MgO + CO_2$. In the two cases, X-ray diffraction (XRD) patterns collected at comparable pressure (P) and temperature (T) (about 80 GPa–2,400 K) show several new peaks that cannot be attributed to the known structures of MgO and CO_2 oxides nor to magnesite. Rather, they indicate that a new structure is stabilized in this pressure range. A typical XRD pattern of the assemblage of $MgO + CO_2$ obtained at 82 GPa and $2{,}350 \pm 150$ K is shown in Fig 1*A*. Upon quenching to room temperature, the high-pressure phase is back-transformed to the low-pressure magnesite structure. Electron energy loss spectroscopy (EELS) analyses performed on the recovered samples are consistent with in situ observations. Fig. 1*B* shows an EELS spectrum collected at the C K-edge on the recovered sample made from the assemblage $MgO + CO_2$. The sharp peak located at 290.3 eV is characteristic of $(CO_3)^{2-}$ carbonate groups (21). In addition, the measured stoichiometry deduced by EELS analysis indicates an $MgCO_3$ composition. Therefore, the high-pressure phase is an isochemical polymorph of magnesite.

Above 80 GPa, natural siderite-rich samples transformed at 1,850–2,300 K yield XRD reflections similar to those obtained in the $MgCO_3$ samples described above, together with reflections of an iron oxide (Fig. 2*A*). This suggests the formation of a high-pressure carbon-bearing phase on the Mg-Fe join. In contrast with the $MgCO_3$ end member, this high-pressure Fe-bearing structure is quenchable. Subsequent transmission electron microscopy (TEM) analyses made on the recovered sample show the presence of three different phases: a relic of untransformed $(Fe_{0.75}Mg_{0.25})CO_3$ siderite, the high-pressure phase, and an iron oxide (Fig. 2*B*). EELS spectra obtained at iron $L_{2,3}$ edges are presented in Fig. 2*C*; some spectra match well with a remnant siderite crystal, with features similar to $Fe^{(II)}$ bearing phase's spectra obtained with the same energy resolution (22). The pre-

Author contributions: E.B., F.G., and G.F. designed research; E.B., A.C., D.A., A.-L.A., J.-P.P., F.G., and G.F. performed research; A.G. and J.-P.P. contributed new reagents/analytic tools; E.B., A.G., F.G., and G.F. analyzed data; E.B., A.G., A.C., D.A., A.-L.A., J.-P.P., F.G., and G.F. wrote the paper.

The authors declare no conflict of interest.

This article is a PNAS Direct Submission.

[1]To whom correspondence should be addressed. E-mail: boulard@impmc.jussieu.fr.

This article contains supporting information online at www.pnas.org/lookup/suppl/doi:10.1073/pnas.1016934108/-/DCSupplemental.

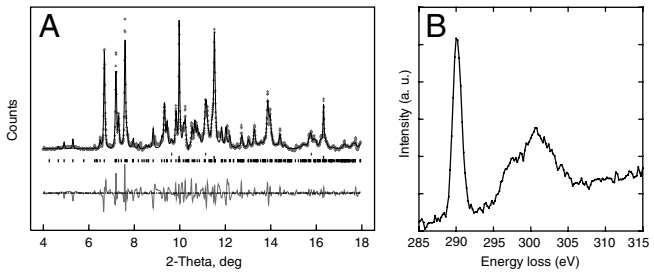

Fig. 1. (*A*) X-ray diffraction pattern of a sample obtained from the transformation of periclase in CO_2 confining medium at 82 GPa and 2,350 ± 150 K. Crosses represent observed data after subtraction of the background and the solid line represents the profile refinement. For this refinement we used an assemblage of untransformed periclase (*Upper*), platinum (*Middle*), and the new high-pressure phase (*Lower*). Residual between observations and fit is shown below the spectrum. (*B*) C K-edge EELS spectrum done on the recovered sample.

sence of magnetite is also confirmed with our EELS analysis. The fine structure of the Fe $L_{2,3}$-edges of the high-pressure phase shows unambiguously fine structures expected in $Fe^{(III)}$-bearing minerals (22, 23) and quantification according to ref. 24 shows that at least about ¾ of iron is present under the $Fe^{(III)}$ oxidation state. EELS data from the C K-edge (Fig. 2*D*) confirm the presence of a remnant siderite and show a spectroscopic signature for the transformed carbonate with a main peak shifted at 290.7 eV. The smaller peak at 287.5 eV corresponds to the presence of carbon monoxide (CO) (25) probably present as inclusions/nanobubbles that give the particular microstructure of this high-pressure phase (Fig. 2*B*). As discussed below, these inclusions are produced during the formation of the high-pressure polymorph of carbonate. EELS measurements indicate element ratios that are different from the initial carbonate: $Fe/C \sim 0.61 \pm 0.07$ and $Fe/O \sim 0.22 \pm 0.02$.

Transformation of $(Mg_{0.6},Fe_{0.4})O + CO_2$ at 105 GPa and ~2,850 K led to the formation of the assemblage of a relic of unreacted material $(M_{0.6},Fe_{0.4})O$, a high-pressure phase of magnetite and the same new high-pressure phase. This assemblage was observed by X-ray diffraction (XRD) and further confirmed by analytical transmission electron microscopy (Fig. 3*A*). Nanodiamonds were also identified by electron diffraction and EELS spectroscopy performed at the C K-edge (Fig. 3*B*).

Discussion

Refinement of the high-pressure and high-temperature XRD patterns allowed the identification of the high-pressure carbon-bearing structure. XRD patterns are consistent with phase II of magnesite (space group C2/m) suggested by theoretical calculations within this pressure range (15). However, the quality of the fit is considerably improved when using instead a slightly less symmetric lattice with space group P21/c (Table S1). This structure shown in Fig. 4 is made of groups of three $(CO_4)^{4-}$ tetrahedra sharing one corner, which constitute $(C_3O_9)^{6-}$ rings. The lattice parameters are $a = 8.39$ Å, $b = 6.41$ Å, $c = 6.82$ Å, $\beta = 105.49°$ ($V = 354.7$ Å^3) in the case of $MgO + CO_2$ at $P = 82$ GPa and $T = 2{,}350 \pm 150$ K and $a = 8.37$ Å, $b = 6.37$ Å, $c = 6.80$ Å, $\beta = 104.57°$ ($V = 351.7$ Å^3) in the case of $MgCO_3$ at $P = 85$ GPa and $T = 2{,}400 \pm 150$ K (Table S2). In that latter case, assuming a number of formula unit per cell of 12 (15), a density of 4.76 g/cm^3 is obtained corresponding to a density difference of about +10% with respect to the low-pressure structure at the same P-T conditions. Because of the incorporation of relatively smaller $Fe^{(III)}$ atoms, the volume of the new Fe-bearing phase is about 10% smaller than the one of the magnesian end member (Table S2) for which we obtained $a = 7.72$ Å, $b = 6.41$ Å, $c = 6.57$ Å, $\beta = 101.31°$ ($V = 319.0$ Å^3) in the case of $(Mg_{0.6}Fe_{0.4})O + CO_2$ at $P = 105$ GPa and $T = 2{,}850 \pm 150$ K and $a = 7.83$ Å, $b = 6.37$ Å, $c = 6.73$Å, $\beta = 101.97°$ ($V = 328.9$ Å^3) in the case of $(Mg_{0.25}Fe_{0.75})CO_3$ at $P = 80$ GPa and room temperature.

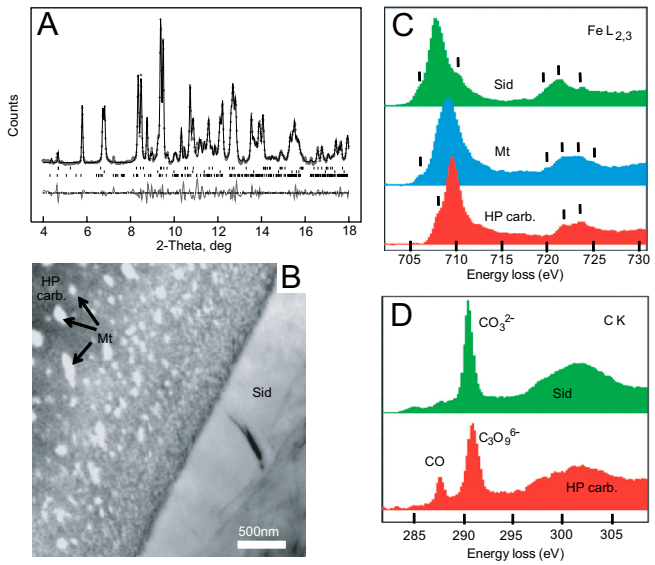

Fig. 2. (*A*) X-ray diffraction pattern collected at 80 GPa and room temperature of siderite transformed at 1,850–2,300 K. Crosses represent observed diffraction data after subtraction of the background and solid line the profile refinement. For the refinement we used an assemblage of high-pressure polymorph of magnetite (37) (*Upper*), untransformed siderite (space group R-3c) (*Middle*), and the new high-pressure phase (*Lower*). Residual between observations and fit is shown below the spectrum. (*B*) STEM high-angle annular dark field showing the untransformed siderite (Sid), the iron oxide (Mt for magnetite), and the transformed carbonate (HP carb.) appearing as a dark gray uniform matrix in the left side of the image. (*C*) EELS spectra collected on the recovered sample. These spectra provide qualitative information on the $Fe^{(III)}/\sum Fe$ ratio of each phase (23, 24) and noticeable features have been indicated by small bars and can be compared with reference siderite, magnetite, and $Fe^{(III)}$ oxide (22). Spectrum collected on the untransformed carbonate shows a high intensity peak of 707.7 eV that indicates the main iron speciation to be $Fe^{(II)}$. In the case of the iron oxide, the broad L_3 peak at 707–709 eV with no splitting is characteristic of magnetite, whereas the L_2 shows many subsplitting and an intermediate energy position between pure ferric and ferrous iron that is typical of a mixed valence of magnetite (23). The spectrum collected in the new phase shows a L_3 line at higher energy loss than in carbonate groups with a fine structure indicating the main iron speciation to be $Fe^{(III)}$. (*D*) C K-edge spectra collected in the untransformed and transformed carbonate phases. In the case of siderite relic, the peak at 290.3 eV corresponds to planar $(CO_3)^{2-}$ carbonate groups. In the spectrum collected in the transformed carbonate, the slightly broader peak at 290.7 eV is attributed to the tetrahedral $(CO_4)^{4-}$ forming rings of $(C_3O_9)^{6-}$. Presence of CO can also be detected in intimate association with the new phase.

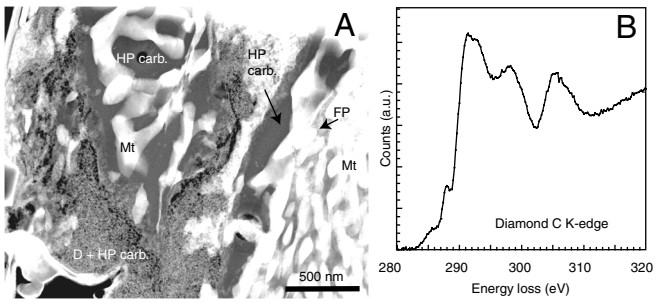

Fig. 3. (*A*) TEM image of the recovered sample from the ferropericlase+CO_2 experiment. Magnetite (Mt), high-pressure carbon-bearing phase (HP carb.), ferropericlase (FP), and nanodiamonds (D) are present. (*B*) C K-edge EELS spectrum of nanodiamonds observed in the recovered sample. The spectrum presents the absorption edge at 289 eV and the dip at 303 eV is characteristic of diamond C K-edge (38, 39).

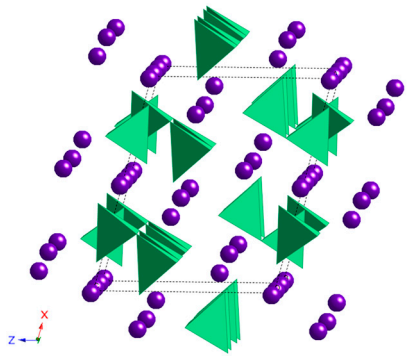

Fig. 4. Structure of the new high-pressure phase in space group P21/c related to phase II of magnesite proposed by theoretical calculation (15). $(CO_4)^{4-}$ tetrahedra appear in green and magnesium atoms are shown as violet spheres.

Because no reference of EELS spectra exist for that new high-pressure phase, density functional theory (DFT) calculations of the unoccupied electronic density of state have been performed. The magnesite density of state shows a narrow peak at around 5 eV above the Fermi level that corresponds to the observed C K-edge and its "molecular" style $(CO_3)^{2-}$ signature (Fig. 5). The density of state obtained for the new high-pressure carbon-bearing phase does not show any molecular $(CO_3)^{2-}$ peak but rather a broad band at higher energy (from 7 to 11 eV). The crystal density is of 4.79 $g \cdot cm^{-3}$ at a pressure of 80 GPa. The geometry of $(C_3O_9)^{6-}$ rings can be seen on the right-hand side of Fig. 5.

In order to see how the tetrahedral $(C_3O_9)^{6-}$ rings change during the decompression, structures have been relaxed at ambient conditions. The result obtained is shown at the bottom (density is 3.60 $g \cdot cm^{-3}$) and the C-O bond lengths increase. From 80 GPa to 0 GPa the C-O-C angle also evolves from around 110–112° to 115–118°, which are values in agreement with published tetrahedral distortion (15). These structural changes have a strong influence on the unoccupied density of state. Indeed, as expected for less dense structures, the overall unoccupied density of state shifts to lower energy. Narrow peaks are present and correspond to tetrahedral $(C_3O_9)^{6-}$ rings, whose molecular signatures are similar to those observed by EELS in samples recovered from high-pressure experiments (i.e., a peak observed at around 290.7 eV).

In Fe-bearing experiments, a large amount of $Fe^{(III)}$ is incorporated in the new structure. No Pt was present in these experiments, and thus Pt had no interference with this redox reaction. The redox partner for $Fe^{(III)}$ formation could eventually be $Fe^{(0)}$ as observed for high-pressure silicates such as perovskite (9). $Fe^{(0)}$ may have been an intermediate partner; however, no evidence of $Fe^{(0)}$ was observed in the recovered samples. We argue that the incorporation of $Fe^{(III)}$ is more likely due to an oxidized carbon partner. We propose that oxidation of iron is balanced by partial reduction of carbon-bearing molecular structures such as $(CO_3)^{2-}$ or CO_2, according to the following chemical reaction:

$$20(Mg_{0.25}Fe^{(II)}{}_{0.75})CO_3 = 20Mg_{0.25}Fe^{(III)}{}_{0.3}(C_3O_9)_{0.233} + 3Fe_3O_4 + 6CO \text{ [or } 3(C + CO_2)\text{]}. \quad \textbf{[1]}$$

This reaction implies an elemental ratio of $Fe/C \sim 0.43$ and $Fe/O \sim 0.14$ in the new $Fe^{(III)}$-bearing phase, in reasonable agreement with EELS estimations on the recovered sample.

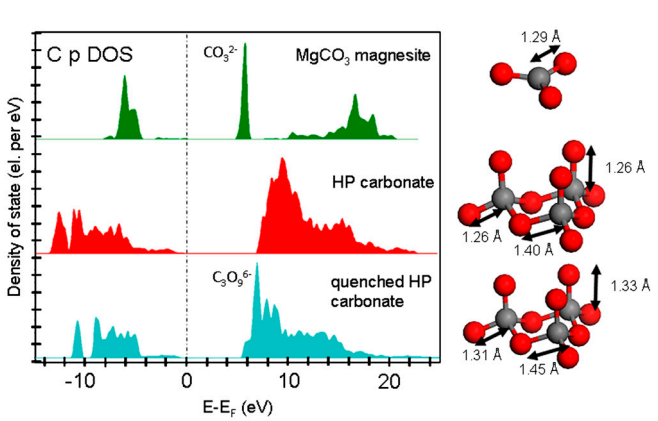

Fig. 5. DFT calculations for electronic density of state of the carbon atoms (p orbital symmetry). This unoccupied density of state roughly corresponds to the excitation probed by EELS at the C K-edge (excitonic effects are neglected in the calculation).

Conclusion

Our study provides direct evidence for the recombination of CO_2 with other oxides to form a high-pressure carbon-bearing phase at P-T conditions close to the lower mantle geotherm. This suggests a strong stability of this phase against dissociation into simple oxides. Also, the preference of the new high-pressure phase for $Fe^{(III)}$ implies reduction of part of the carbon, following the chemical reaction **1**. It shows experimentally the coexistence of oxidized and reduced species of carbon at lower mantle conditions. This behavior might be due to a strong thermodynamic stability of the new carbon-bearing phase. However, for this new phase to be actually present in the deep lower mantle, carbonates must be preserved during deep subduction. Although the lower mantle assemblage is speculated to induce reducing conditions (9), carbonates could remain stable at depths if isolated from the surrounding mantle, for instance, in a relatively cold subducted slab where oxygen fugacity, as controlled by the local mineral assemblage, is locally higher (10, 26). This fraction of surviving carbonates may be transported beyond 1,800-km depth, where transformation into the newly observed $Fe^{(III)}$-bearing phase would occur.

Materials and Methods

Two types of experiments have been conducted, with starting materials being either natural carbonate samples or a stoichiometric intimate assemblage of pure oxides. Grounded natural carbonates of two compositions on the iron-magnesium join, $MgCO_3$ magnesite and $(Fe_{0.75}Mg_{0.25})CO_3$ siderite, were provided by the mineralogical collection of University of Pierre et Marie Curie and loaded in symmetric Mao-type diamond-anvil cell without a pressure-transmitting medium. Clear inclusion-free crystals were chosen and analyzed by electron microprobe showing very little minor elements content (Table S3). Moreover, in order to test the recombination of oxides, synthetic periclase (MgO) and ferropericlase $(M_{0.6},Fe_{0.4})O$ were loaded into CO_2 gas. For Mg end-member experiments using $MgCO_3$ and MgO as starting material, finely ground powdered platinum (platinum black) was incorporated and used as infrared absorber. Samples were pressurized at ambient temperature and then heated using the double-sided heating system available on the high-pressure beam line ID-27 at the European Synchrotron Radiation Facility (ESRF) (27). Hot spots developed on the sample (and transformed areas) are of the order of 20 μm in diameter. Angle dispersive XRD pattern were collected in situ at high pressure and at high temperature, with a beam focused down with Kirkpatrick–Baez mirrors to 1.7 × 2.3 μm FWHM at 33.3 keV (wavelength of 0.3738 Å), so as to minimize the influence of lateral temperature gradients in X-ray diffraction patterns. Typical exposure time was about 90 s at high pressure–high temperature. About 2 h of heating at 2,000–2,500 K were applied to transform the samples. Pressure was measured using ruby fluorescence at room temperature (28) and the thermal equation of state of platinum (29) at high temperature. Temperatures were measured by spectroradiometric analysis of thermal emission spectra (30). The diffraction images were integrated with the Fit2d software (31), and the one-dimensional diffraction patterns were processed with the GSAS software package (32) using the LeBail method to identify phases and determine lattice parameters.

Analyses of recovered samples were carried out on carefully selected regions of interest, at the center of transformed area. The recovered samples

were then thinned to electron transparency (~100 nm) by the focused ion beam (FIB) method prior to observations in scanning transmission electron microscopy (STEM) and TEM. FIB milling was performed with a FEI STRATA DB 235 at Institut d'Electronique, de Microélectronique et de Nanotechologie (IEMN) and Zeiss Crossbeam Neon40 at Institut de Minéralogie et de Physique des Milieux Condensés (IMPMC). To protect the sample during the milling process, a linear strap of platinum was deposited across the heated area, localized by the electronic imaging capabilities of the FIB. A 30-kV Ga^+ beam operating at ~20 nA was used to excavate a thin foil, removing sample material on both sides of the platinum layer to a depth of 5–10 μm. The thin cross-sections (15 μm × 5 μm × 1 μm) were extracted using a micromanipulator and welded to a TEM copper grid. Final thinning down to a thickness of less than 100 nm was achieved using low incident angles and low Ga ion currents (approximately 50 pA). A further description of the FIB sample preparation technique can be found in Heaney et al. (33).

Transmission electron microscopy was done with a JEOL 2100-F operating at 200 kV with a field effect gun as electron source. STEM-EELS measurements were done with a dedicated scanning transmission electron microscope Vacuum Generators HB 501 microscope. All EELS spectra were recorded in STEM mode with 100-keV incident electrons focused on the specimen. The probe size was of *ca.* 1 nm and the current intensity of 100 pA. The collection semiangle and the convergent semiangle of this microscope are, respectively, of 24 mrad and 7 mrad. The electronic structures of each element were investigated using EELS spectra collected at the C K-, O K-, and Fe $L_{2,3}$-edges with an energy dispersion of 0.2 eV per channel. The final energy resolution measured as the width of the zero-loss peak at half height was of 0.6 eV. We used the Hitchcock gas core excitation database and already published fingerprint of EELS data for identification and interpretation of fine structure EELS spectra of the different elements (Fe and C).

DFT has also been performed in order to interpret the C K-edges of the newly reported structure. The DFT calculations were performed for the Mg end-member carbonate using a pseudopotential method (valence electrons are C $2s^2$ $2p^2$, O $2s^2$ $2p^4$, and Mg $2p^6$ $3s^2$) and a plane wave basis with an energy cutoff at the order of 1,000 eV (34, 35). Because no iron atoms were included in the structure, non-spin-polarized local density approximation has been used as an exchange-correlation functional, and site and symmetry projected density of state has been computed using the tetrahedron method. Structural models have been relaxed (residual atomic forces below 5.10^{-3} eV/Å) in order to obtain the quenched structure for the high-pressure phase. An indicative stoichiometry of the new phases was obtained using a conventional extraction and Hartree–Slater cross–section calculation (36). This method provides us cation ratios such as Fe/C, Fe/O, and C/O. The reliability of this method was first verified on different natural carbonates composition, and the measured stoichiometries were in good agreement with electron microprobe analysis.

ACKNOWLEDGMENTS. The authors thank J. C. Boulliard from the mineralogical collection of Université Pierre et Marie Curie and P. Munsch, G. Lemarchand, and H. Ozawa for their help with experiments and cell loadings. D. Troadec and I. Machouk are acknowledged for their help with FIB sample preparation and N. Menguy for discussions and advice on FIB sample analyses. The FIB and SEM facility of IMPMC is supported by Région Ile de France Grant SESAME 2006 NOI-07-593/R, INSU-CNRS, INP-CNRS, University Pierre et Marie Curie-Paris 6, and by the French National Research Agency (ANR) Grant ANR-07-BLAN-0124-01. A.C. acknowledges support from the European Research Council under European Community's seven framework program (FP7/2007-2013)/ERC Grant 207467. Two anonymous reviewers and the editor are warmly thanked for their help in strongly improving the quality of the manuscript.

1. Sleep NH, Zahnle K (2001) Carbon dioxide cycling and implications for climate on ancient Earth. *J Geophys Res-Planet* 106:1373–1399.
2. Javoy M (1997) The major volatile elements of the Earth: Their origin, behavior, and fate. *Geophys Res Lett* 24:177–180.
3. Lecuyer C, Simon L, Guyot F (2000) Comparison of carbon, nitrogen and water budgets on Venus and the Earth. *Earth Planet Sci Lett* 181:33–40.
4. Keppler H, Wiedenbeck M, Shcheka SS (2003) Carbon solubility in olivine and the mode of carbon storage in the Earth's mantle. *Nature* 424:414–416.
5. Shcheka SS, Wiedenbeck M, Frost DJ, Keppler H (2006) Carbon solubility in mantle minerals. *Earth Planet Sci Lett* 245:730–742.
6. Biellmann C, Gillet P, Guyot F, Peyronneau J, Reynard B (1993) Experimental evidence for carbonate stability in the Earth's lower mantle. *Earth Planet Sci Lett* 118:31–41.
7. Fiquet G, et al. (2002) Structural refinements of magnesite at very high pressure. *Am Mineral* 87:1261–1265.
8. Isshiki M, et al. (2004) Stability of magnesite and its high-pressure form in the lowermost mantle. *Nature* 427:60–63.
9. Frost DJ, McCammon CA (2008) The redox state of Earth's mantle. *Annu Rev Earth Planet Sci* 36:389–420.
10. Ballhaus C, Berry RF, Green DH (1990) Oxygen fugacity controls in the Earth's upper mantle. *Nature* 348:437–440.
11. Haggerty SE (1999) Earth and planetary sciences—A diamond trilogy: Superplumes, supercontinents, and supernovae. *Science* 285:851–860.
12. Torsvik TH, Burke K, Steinberger B, Webb SJ, Ashwal LD (2010) Diamonds sampled by plumes from the core-mantle boundary. *Nature* 466:352–355.
13. Brenker FE, et al. (2007) Carbonates from the lower part of transition zone or even the lower mantle. *Earth Planet Sci Lett* 260:1–9.
14. Stachel T, Harris JW, Brey GP, Joswig W (2000) Kankan diamonds (Guinea) II: Lower mantle inclusion parageneses. *Contrib Mineral Petr* 140(1):16–27.
15. Oganov AR, Ono S, Ma YM, Glass CW, Garcia A (2008) Novel high-pressure structures of $MgCO_3$, $CaCO_3$ and CO_2 and their role in Earth's lower mantle. *Earth Planet Sci Lett* 273:38–47.
16. Panero WR, Kabbes JE (2008) Mantle-wide sequestration of carbon in silicates and the structure of magnesite II. *Geophys Res Lett* 35:L14307, 10.1029/2008GL034442.
17. Skorodumova NV, Belonoshko AB, Huang L, Ahuja R, Johansson B (2005) Stability of the $MgCO_3$ structures under lower mantle conditions. *Am Mineral* 90:1008–1011.
18. Santillan J, Williams Q (2004) A high-pressure infrared and X-ray study of $FeCO_3$ and $MnCO_3$: Comparison with $CaMg(CO_3)_2$-dolomite. *Phys Earth Planet In* 143–144: 291–304.
19. Lavina B, et al. (2009) Siderite at lower mantle conditions and the effects of the pressure-induced spin-pairing transition. *Geophys Res Lett* 36:L23306, 10.1029/2009GL039652.
20. Mattila A, et al. (2007) Pressure induced magnetic transition in siderite $FeCO_3$ studied by x-ray emission spectroscopy. *J Phys Condens Matt* 19:386206, 10.1088/0953-8984/19/38/386206.
21. Hofer F, Golob P (1987) New examples for near-edge fine-structures in electron-energy loss spectroscopy. *Ultramicroscopy* 21:379–383.
22. Gloter A, Douiri A, Tence M, Colliex C (2003) Improving energy resolution of EELS spectra: An alternative to the monochromator solution. *Ultramicroscopy* 96:385–400.
23. Paterson JH, Krivanek OL (1990) ELNES of 3d transition-metal oxides. 2. Variations with oxidation state and crystal structure. *Ultramicroscopy* 32(4):319–325.
24. van Aken PA, Liebscher B, Styrsa VJ (1998) Quantitative determination of iron oxidation states in minerals using Fe L-2,L-3-edge electron energy-loss near-edge structure spectroscopy. *Phys Chem Miner* 25:323–327.
25. Hitchcock AP, Brion CE (1980) *K*-Shell excitation spectra of CO, N_2 and O_2. *J Electron Spectrosc* 18:1–21, Database of core excitation spectra: http://unicorn.mcmaster.ca/corex.html.
26. Dasgupta R, Hirschmann MM, Whiters AC (2004) Deep global cycling of carbon constrained by the solidus of anhydrous, carbonated eclogite under upper mantle conditions. *Earth Planet Sci Lett* 227:73–85.
27. Mezouar M, et al. (2005) Development of a new state-of-the-art beamline optimized for monochromatic single-crystal and powder X-ray diffraction under extreme conditions at the ESRF. *J Synchrotron Radiat* 12:659–664.
28. Mao HK, Xu J, Bell PM (1986) Calibration of the ruby pressure gauge to 800-kbar under quasi-hydrostatic conditions. *J Geophys Res-Solid* 91:4673–4676.
29. Fei YW, et al. (2007) Toward an internally consistent pressure scale. *Proc Natl Acad Sci USA* 104:9182–9186.
30. Benedetti LR, Loubeyre P (2004) Temperature gradients, wavelength-dependent emissivity, and accuracy of high and very-high temperatures measured in the laser-heated diamond cell. *High Pressure Res* 24:423–445.
31. Hammersley AP, Svensson SO, Hanfland M, Fitch AN, Hausermann D (1996) Two-dimensional detector software: From real detector to idealised image or two-theta scan. *High Pressure Res* 14:235–248.
32. Larson AC, Von Dreele RB (1994) General structure analysis system (GSAS). *Los Alamos National Laboratory Report LAUR* pp 86–748.
33. Heaney PJ, Vicenzi EP, Giannuzzi LA, Livi KJT (2001) Focused ion beam milling: A method of site-specific sample extraction for microanalysis of Earth and planetary materials. *Am Mineral* 86:1094–1099.
34. Gonze X, et al. (2009) ABINIT: First-principles approach to material and nanosystem properties. *Comput Phys Commun* 180:2582–2615.
35. Gonze X, et al. (2002) First-principles computation of material properties: The ABINIT software project. *Comp Mater Sci* 25:478–492.
36. Egerton RF, ed. (1996) *Electron Energy-Loss Spectroscopy in the Electron Microscope* (Springer, Berlin) p 500.
37. Haavik C, Stolen S, Fjellvag H, Hanfland M, Hausermann D (2000) Equation of state of magnetite and its high-pressure modification: Thermodynamics of the Fe-O system at high pressure. *Am Mineral* 85:514–523.
38. Batson PE, Bruley J (1991) Dynamic screening of the core exciton-energy-loss scattering. *Phys Rev Lett* 67:350–353.
39. Morar JF, Himpsel FJ, Hollinger G, Hughes G, Jordan JL (1985) Observation of a C 1 s core exciton in diamond. *Phys Rev Lett* 54:1960–1963.